

Plasmon-Matter Interactions in Optoelectronic Metamaterials with Negative Refractive Index

Jinjin Xie · Qingyan Fan · Fuchun Xi · Hong Xiao ·
Ziao Tian · Lijian Zhang · Jie Xu · Qijun Ren ·
Lei Zhou · Paul K. Chu · Zhenghua An

Received: 10 November 2012 / Accepted: 25 February 2013 / Published online: 27 March 2013
© Springer Science+Business Media New York 2013

Abstract Optoelectronic metamaterials composed of nanoscale metallic structures and semiconductor quantum structures constitute a powerful platform to explore light-matter interaction and new devices. In this work, we numerically study an optoelectronically coupled metamaterial consisting of metallic double fishnet (DF) layers and semiconductor quantum well (QW) spacing layer. When the electronic intersubband transition (ISBT) in the QW coincides with the plasmonic resonances of the DF structure, the plasmon-matter interaction (PMI) can modify the optical properties considerably. In case of the ISBT-matching localized surface plasmons (LSP), i.e., $f_{\text{QW}}=f_{\text{LSP}}$, the polarization-selection-rule forbidden ISBT absorption can be enabled due to the nonnegligible E_z field distributions while the retrieved optical constants remain almost unchanged. However, when the gap surface plasmons (GSP) are matched, i.e., $f_{\text{QW}}=f_{\text{GSP}}$, PMI exhibits a clear anti-crossing behavior implying strong coupling effects between ISBT and GSP resonance and formation of intersubband polaritons. The effective optical constants are therefore modulated appreciably. The large difference between GSP and LSP can be attributed to their distinctive resonance qualities (Q-factors) and polarization conversion ratios (99.28 % for GSP and 1.54 % for LSP) from the transverse electric (TE) to transverse magnetic (TM) mode. Our results provide insight into the physical mechanism of PMI in nanoscale semiconductor-plasmon

hybrid systems and suggest an alternative means in tunable negative refractive index (NRI) applications.

Keywords Plasmon-matter interactions (PMIs) · Negative refractive index (NRI) · Localized surface plasmons (LSP) · Gap surface plasmons (GSP) · Intersubband transition (ISBT)

Introduction

Light-matter interactions (LMIs) [1] or more specifically, light-semiconductor interactions (LSIs) [2], are fundamentally important subjects in condensed matter physics and optoelectronic applications. With many fascinating phenomena [1, 3, 4] many devices such as lasers [5], modulators [6], and photodetectors [7] have been demonstrated. The LSI strength can be strongly enhanced by embedding the active semiconductor into optical structures such as Fabry-Perot [8] or distributed feedback (DBR) cavities [2], photonic crystals (PCs) [9], or metamaterials (MTMs) [10]. In this way, the strong coupling regime of LMIs can be reached and the photon modes and electronic states are hybridized to generate new half-electron and half-photon eigenstates or polaritons [2]. Among these structures, MTMs are particularly useful and allow manipulation of the optical fields rendered by electromagnetic waves and therefore, the optical constants of these artificial materials can be engineered. Particularly, negative refractive index (NRI) materials (with both permittivity and permeability being tuned to be negative) [11] have attracted much research interest due to promising applications such as super- or hyper-focusing, subwavelength imaging, cloaking, and transformation optics [12]. The surface plasmons in these NRI materials are known to exhibit large field-enhancement and strong energy localization effects and they should be highly desirable in boosting LMI strength. However, to the best of our

J. Xie · Q. Fan · F. Xi · H. Xiao · Z. Tian · L. Zhang · J. Xu ·
Q. Ren · L. Zhou · Z. An (✉)
Institute of Advanced Materials and State Key Laboratory
of Surface Physics, Fudan University, Shanghai 200433,
People's Republic of China
e-mail: anzhenghua@fudan.edu.cn

P. K. Chu
Department of Physics and Materials Science,
City University of Hong Kong, Tat Chee Avenue,
Kowloon, Hong Kong, China

knowledge, there have been few reports [13] utilizing NRI structures to regulate the LMI or LSI strength in semiconductors with resonant electronic transitions or quantum media in general. Hence, in semiconductor-coupled NRI materials, the plasmon-matter interaction (PMI) mechanisms remain elusive and the optical properties of this hybrid system are not well-known, despite increasing research interest from the scientific community [2, 5, 11, 13–15].

On the heels of the discovery of possible exotic optical properties, the combination of NRI structures and semiconductors may open a promising route to produce tunable NRI materials and can greatly expand the functionalities and applications of existing NRI materials. Several tunable systems composed of liquid crystals [16] and superconductors [17] have already been researched and the prototypic electrically or optically tunable NRI components demonstrated. Compared to these systems, semiconductor (nano-) structures are more desirable [18] due to versatile band-gap engineering and excellent controllability of the carrier behavior. In addition, the mature and advanced (nano-) fabrication techniques assure good integration between semiconductors and NRI structures. In fact, loss compensation has been achieved from NRI materials by utilizing optical gains in semiconductor nanostructures [15, 19–21].

In this work, we investigate a typical NRI structure, double fishnet (DF), and integrate it into semiconductor quantum-well (QW) materials. The optical properties of the hybrid structures are studied by full-wave simulation and the interactions between NRI-related plasmons and electronic intersubband transitions (ISBT) in semiconductor QWs are investigated. To our surprise, different coupling behavior between the gap surface plasmon (GSP) and localized surface plasmon (LSP) modes with QW ISBT is revealed. Our results not only provide insight into the physical mechanisms of PMI but also contribute to the design and realization of tunable NRI applications involving variable superfocusing [12] and tunable slow-light [22].

Structure and Simulation Method

As shown in Fig. 1, the optoelectronic metamaterial consists of a metal/semiconductor/metal tri-layer with two identical fishnet metal layers (i.e., DF structure) perforated with periodic rectangular holes and a semiconductor spacing layer comprising multiple GaAs/AlGaAs QWs (for simplicity, only one QW is displayed in Fig. 1). The DF structure provides effective electrical and magnetic resonances giving rise to the NRI response. The optical characteristics of the DF structure can be adjusted by varying the geometric parameters [23]. Meanwhile, the quantum-confined energy levels in the QWs can produce ISBT which can also be controlled by bandgap engineering [24]. The exceptionally

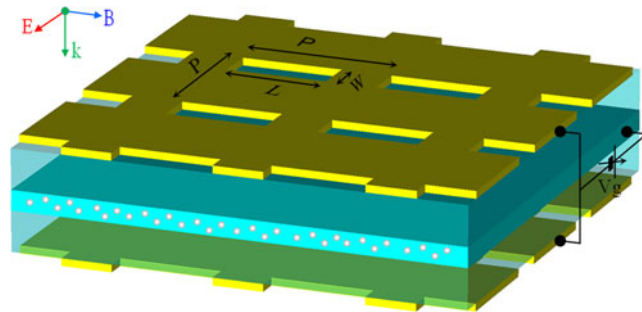


Fig. 1 (Color online) Illustration of the periodic double-fishnet structure with rectangular holes. The sandwiched semiconductor consists of GaAs/AlGaAs multi-layers and the electron density (N_{QW}) in GaAs QW can be adjusted by proper gating (V_g). Dimensions are given in the text

high freedom in the design of this hybrid system is therefore obvious. Besides the “engineerable” ISBT in the QWs, the electron density (N_{QW}) in the QWs can be adjusted electrically by the gating V_g as shown in Fig. 1 even in the post-fabrication stage. In the real fabrication of this tri-layer structure, the layer-transfer technique can be utilized as well [25].

Without losing generality, we adopt the following parameters in this work. The hole array has a fixed lattice constant of $P=3 \mu\text{m}$ and the rectangular holes have a length of $L=2.6 \mu\text{m}$ and width of $W=0.8 \mu\text{m}$. The thicknesses of the metals and semiconductor are $h_m=0.15 \mu\text{m}$ and $h_d=0.40 \mu\text{m}$, respectively. These parameters are chosen in order that the NRI band shows up in the desired frequency range of 15–30 THz (to be discussed later). These values are somewhat different from those used in other reported work [23] because of the very high dielectric contrast between the spacer ($\epsilon_{\text{GaAs}}=12.9$) and surrounding media ($\epsilon_{\text{vacuum}}=1$). In order to take into account the QW ISBT, we apply a Lorenzian model [26] to the permittivity (ϵ_z) of the semiconductor QWs, i.e.,

$$\epsilon_z(f) = \epsilon_{\text{GaAs}} + \frac{N_{\text{QW}} e^2 f_{\text{osc}}}{4\pi^2 m_0 \epsilon_0 L_{\text{eff}}} \frac{1}{(f_{\text{QW}}^2 - f^2) - i\gamma f} \quad (1)$$

in which e is the electron charge, $f_{\text{osc}} = (4\pi m_0/\hbar) f_{\text{QW}} d^2$ is the ISBT oscillator strength of the QWs, L_{eff} is the effective QW width, m_0 is the electron rest mass, and d is the dipole matrix element between the envelope function of the two subbands set as 2 nm in this work, f_{QW} is the ISBT central frequency which is within the range of 15–30 THz, and γ is the intersubband bandwidth. Typically, γ/f_{QW} is smaller than 20 % for bound-to-bound transitions in the experiments [24] and the smallest value is ~1 % [27]. Here, we choose $\gamma/f_{\text{QW}}=5\%$ which should be realizable in practice. With regard to the electron density, based on typical experimental conditions, $N_{\text{QW}}=4.5 \times 10^{11}/\text{cm}^2$ unless otherwise stated. L_{eff} is predetermined by the value of f_{QW} according to bandgap engineering calculation, for instance, $L_{\text{eff}} \approx 10 \text{ nm}$ for $f_{\text{QW}}=$

20 THz. We set $\varepsilon_x = \varepsilon_y = \varepsilon_{\text{GaAs}}$ since the QWs are only sensitive to the E_z component due to the polarization selection rule [24]. The metals are treated as perfect electrical conductor (PEC) since absorption by typical plasmonic metals (Au, Ag, etc.) is negligibly small in this terahertz range [28]. Numerical simulation is performed by the finite-difference time-domain (FDTD) method [29]. A plane wave impacts the structure normally with the E -field polarized along the y -axis, and the reflection and transmission spectra are computed.

Results and Discussion

We begin with the case in which the QWs are fully depleted ($N_{\text{QW}}=0$) and the spacer becomes dispersiveless, i.e., $\varepsilon_{\text{GaAs}}=12.9$. Qualitatively, the result in this case is analogous to the reported DF structure with a vacuum spacer (small ε) [23, 30]. Figure 2a depicts the simulated transmission and reflection spectra. Three characteristic features show up at ~ 20.30 , ~ 21.28 , and ~ 26.85 THz, respectively (vertical dotted lines in Fig. 2a). The transmission dip at $f_{\text{AR}}=20.30$ THz can be assigned to antiresonance (AR). The narrow transmission peak at $f_{\text{GSP}}=21.28$ THz arises from GSP and the broad one at $f_{\text{LSP}}=26.85$ THz originates from LSP. The effective permittivity (ε_{eff}), permeability (μ_{eff}), and refractive indexes (n_{eff} , n_g) retrieved using the reported method [31] are displayed in the lower panels of Fig. 1a. At the LSP frequency ($f=f_{\text{LSP}}$), the effective electrical permittivity ε_{eff} approaches zero implying the electrical response origin of the LSP mode. Below the LSP mode ($f < f_{\text{LSP}}$), the real part of the effective electric permittivity ε_{eff} becomes negative. The

magnetic permeability exhibits strong dispersion around the GSP mode and can be regarded as an anti-symmetric eigenmode of the two coupled metal layers. Hence, it produces effective magnetic response. Above the magnetic eigenfrequency ($f > f_{\text{GSP}}$), the magnetic permeability μ_{eff} turns out to be negative and consequently, both ε_{eff} and μ_{eff} become negative in the frequency range between f_{LSP} and f_{GSP} , leading to a negative (phase) refractive index (NRI), n_{eff} , as shown in Fig. 2a. The simulation results yield a wider NRI band ranging from $f_{\text{AR}} \sim 20.30$ THz to $f_{\text{LSP}} \sim 26.85$ THz [30]. In applications involving fast or slow light [22], the group refractive index (n_g) concerned can be derived from $n_g(\omega) = n_{\text{eff}}(\omega) + \omega \times (\partial n_{\text{eff}}(\omega) / \partial \omega)$. The bottom panel in Fig. 2a depicts the result when $N_{\text{QW}}=0$. It can be observed that n_g is mainly determined by the second term, i.e., the dispersion of n_{eff} . Large n_g values appear at around f_{AR} ($n_g \sim -1,600$) and f_{GSP} ($n_g \sim 320$).

When the QWs are filled with electrons, the ISBT affects the optical properties of the hybrid system. Figure 2b, c display the results of $N_{\text{QW}}=4.5 \times 10^{11} \text{ cm}^{-2}$ with the central frequency of the ISBT fixed at two typical values (b) $f_{\text{QW}}=f_{\text{GSP}}=21.28$ THz and (c) $f_{\text{QW}}=f_{\text{LSP}}=26.85$ THz. For easy comparison, the data for $N_{\text{QW}}=0$ are re-plotted as dotted curves in Fig. 2b, c and the results for $f_{\text{QW}}=f_{\text{LSP}}$ (in Fig. 2c) reproduce all the features in Fig. 2a in terms of both (anti-)resonant positions and broadness of transmission/reflection peaks/dips. This implies that coupling between LSP and ISBT is rather weak. The only discernible difference is the decrease in the magnitude of the transmission peak at $f=f_{\text{LSP}}$ (see top panel of Fig. 2c). The transmission decrease implies certain ISBT absorption. According to the polarization-selection-rule [24], this observed absorption is nontrivial and arises essentially from the mediation by plasmonic resonance between normal incidence and ISBT.

In the case of GSP, i.e., $f_{\text{QW}}=f_{\text{GSP}}$, remarkably different coupling behavior is observed. As shown in Fig. 2b, the transmission valley at the AR redshifts¹ while the GSP-related transmission peak splits into two with a counterintuitive transmission dip/minima between them. Accordingly, the resonant features in the electrical permittivity and magnetic permeability spectra change with excellent correspondence to the transmission/reflection variations. Notably, two negative-permeability frequency ranges appear, and hence, two NRI bands are formed. Effectively, the total NRI bandwidth is expanded. Meanwhile, the amplitude of the real part of n_{eff} is sacrificed (less negative) to a certain extent, suggesting that there is some tradeoff between the NRI bandwidth and amplitude. Owing to the modified n_{eff} dispersion, n_g also exhibits remarkable changes (bottom panel in Fig. 2b). Associated with the above modification, a dip

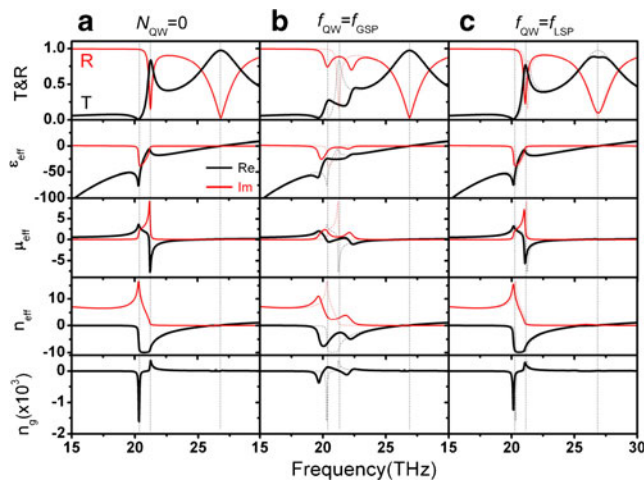
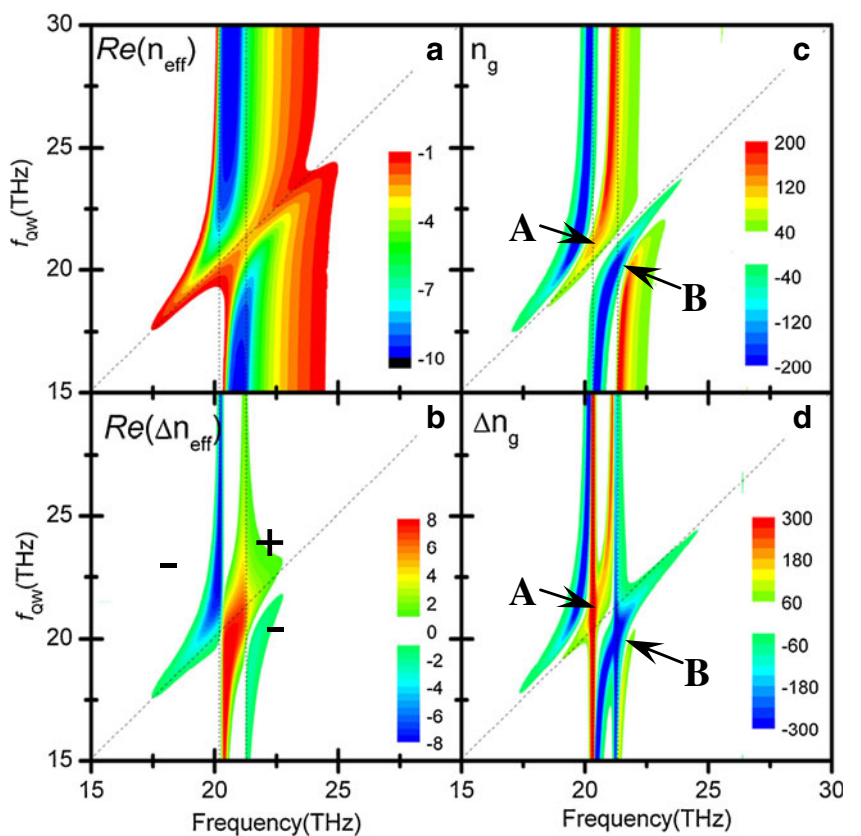


Fig. 2 (Color online) Transmission, reflection spectra and retrieved parameters (ε_{eff} , μ_{eff} , n_{eff} , n_g) for three different cases: **a** Electrons in GaAs QW is fully depleted, i.e., $N_{\text{QW}}=0$; **b**, **c** N_{QW} is fixed to be $4.5 \times 10^{11} \text{ cm}^{-2}$ and intersubband transition frequency (f_{QW}) matches GSP frequency, i.e., $f_{\text{QW}}=f_{\text{GSP}}=21.28$ THz (**b**) and LSP, i.e., $f_{\text{QW}}=f_{\text{LSP}}=26.85$ THz (**c**). The vertical dashed lines indicate, from the left to right, the antiresonance, GSP, and LSP, respectively

¹ More accurately, the AR dip also splits into two, as will be seen later in Fig. 3.

Fig. 3 (Color online) The calculated effective phase and group refractive indexes, i.e., real part of n_{eff} (**a**) and n_g (**c**), when f_{QW} is swept from 15–30 THz with $N_{\text{QW}}=4.5 \times 10^{11} \text{ cm}^{-2}$. Data are re-plotted in **b** and **d** after subtracting the index values for $N_{\text{QW}}=0$, i.e., $\Delta n_{\text{eff}} = n_{\text{eff}}|_{N_{\text{QW}}=4.5 \times 10^{11} \text{ cm}^{-2}} - n_{\text{eff}}|_{N_{\text{QW}}=0}$ (**b**) and $\Delta n_g = n_g|_{N_{\text{QW}}=4.5 \times 10^{11} \text{ cm}^{-2}} - n_g|_{N_{\text{QW}}=0}$ (**d**). Vertical dotted lines in each panel show the antiresonance and GSP, respectively, and sloped dotted lines are guidelines with $f=f_{\text{QW}}$ from which anticrossing behavior can be identified



structure appears in the imaginary part of n_{eff} , which is reminiscent to the well-known electromagnetically induced transparency (EIT) phenomena [32, 33]. The presence of EIT-like feature² implies much stronger coupling between the GSP and ISBT and this issue will be discussed later.

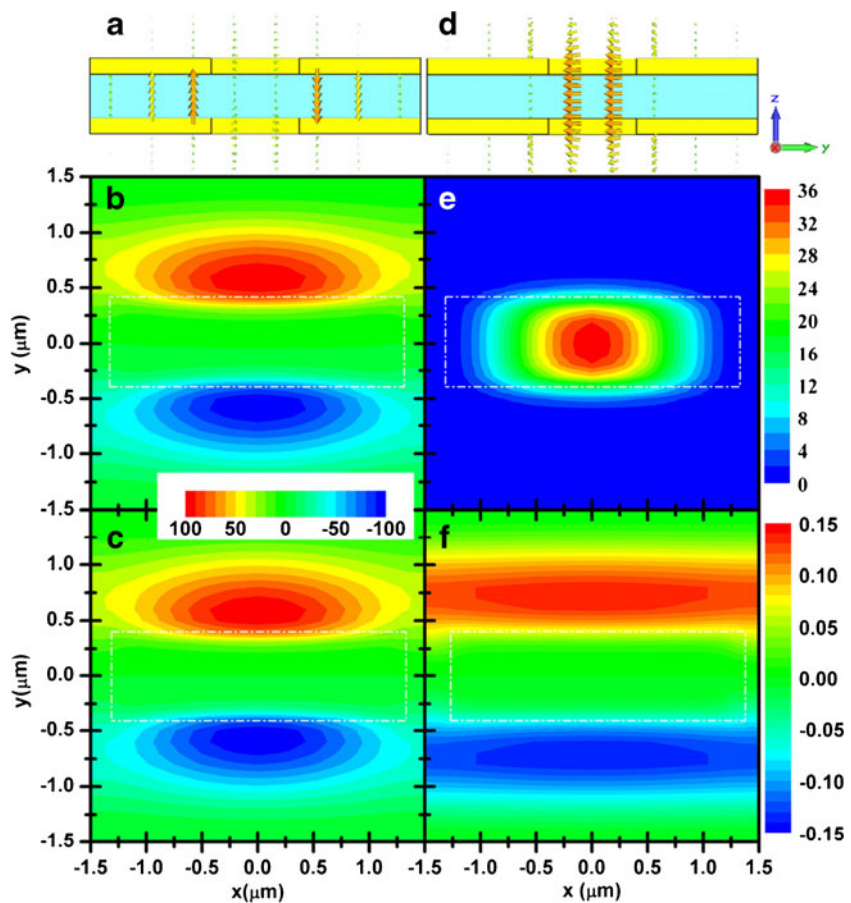
To be more systematic, we fix the geometrical parameters of the DF structure and sweep the detuning between plasmonic (anti)resonances and electronic transitions by varying the ISBT frequency (f_{QW}) in the range of 15–30 THz while keeping a constant N_{QW} ($=4.5 \times 10^{11} \text{ cm}^2$). Detuning between the GSP mode (AR antimode) and QW resonance is defined to be $\delta_{\text{GSP}}=f_{\text{QW}}-f_{\text{GSP}}$ ($\delta_{\text{AR}}=f_{\text{QW}}-f_{\text{AR}}$). In Fig. 3a, the NRI region is displayed in a two-dimensional color-plot as functions of detuning. It is surprising to find that the NRI band exhibits an anticrossing-like behavior when coupled to QWs, although the NRI band itself is not a single-mode eigenstate. We can see that the NRI band morphs into two subbands when f_{QW} crosses f_{AR} and f_{GSP} . In the negative δ_{AR} region, the additional NRI response appears in the vicinity of $f=f_{\text{QW}}$ and similar features appear on the high frequency side of the NRI band (with rather large and positive δ_{GSP}). Between these two ends (i.e., when $|\delta_{\text{GSP}}|$ is not too large), the NRI response is divided into two

adjacent bands and the compromise between total NRI bandwidth and amplitude is apparent. To visualize the ISBT-induced changes, Fig. 3b shows the tuned amplitude of n_{eff} with respect to the depleted QW case ($N_{\text{QW}}=0$), i.e., $\Delta n_{\text{eff}}=n_{\text{eff}}|_{N_{\text{QW}}=4.5 \times 10^{11} \text{ cm}^{-2}} - n_{\text{eff}}|_{N_{\text{QW}}=0}$. Three typical regions are observed. Below the AR mode ($f < f_{\text{AR}}$), Δn_{eff} is negative indicating that negative n_{eff} is generated by QW coupling. In the intermediate region ($f_{\text{AR}} < f < f_{\text{GSP}}$), n_{eff} turns out to be less negative ($\Delta n_{\text{eff}} > 0$) whereas above the GSP mode ($f > f_{\text{GSP}}$), Δn_{eff} shows a more complicated dependence on f_{QW} . It may be ascribed to the influence of the broad LSP mode. Roughly speaking, Δn_{eff} is negative (positive) at small (large) f_{QW} .

The anticrossing behavior is unambiguously demonstrated by the results of group refractive index n_g , as shown in Fig. 3c–d (c, n_g ; d, $\Delta n_g=n_g|_{N_{\text{QW}}=4.5 \times 10^{11} \text{ cm}^{-2}} - n_g|_{N_{\text{QW}}=0}$). Both positive and negative n_g peaks (located at $f \sim f_{\text{GSP}}$ and $f \sim f_{\text{AR}}$, respectively) split into two when coupled to the QW transitions and form two sets of anticrossing branches. The amplitude of the splitting between two asymmetric branches or Rabi-like splitting (D) is evaluated to be as large as ~ 4 THz (for $N_{\text{QW}}=4.5 \times 10^{11} \text{ cm}^2$), implying that the strong coupling effect evolves from the interaction between the ISBT and plasmonic resonance. To the best of our knowledge, this is the first indication of formation of intersubband polaritons arising from interacting ISBT oscillators and metallic plasmons [34, 35]. As a result, n_g changes dramatically. For

² EIT requires two interacting modes or transitions, one is dark and the other bright. In our structure, the QW ISBT happens to be a dark mode to normal incidence while GSP mode is bright one.

Fig. 4 (Color online) Arrow and contour plots of the electric-field distributions of the GSP mode (**a**–**c**) and LSP (**d**–**f**), in yz -plane with $x=0$, **a** and **d**; in xy -plane with $z=0$, (**b**–**c**) and (**e**–**f**). **b** and **e** show the electric-field amplitudes, i.e., $|E|^2/|E_0|^2$, while **c** and **f** display their z -components, i.e., $|E_z|^2/|E_0|^2$. White dotted rectangles indicate the hole positions



example, n_g at $f \sim f_{\text{AR}}$ changes from an initially negative value ($\sim -1,600$) to positive (~ 120) due to coupling with QW electrons (point A in Fig. 3c–d), whereas n_g at $f \sim f_{\text{GSP}}$ changes from positive (~ 260) to negative (~ -180) at point B. It should be noted that the coupling strength is continuously tunable by varying the gate bias (V_g), although the data are not shown here. The Rabi splitting has a dependence on N_{QW} with a relationship of $D \sim (N_{\text{QW}})^{1/2}$ [34]. Therefore, n_g (as well as other optical constants) can be modulated in a wide range depending on the largest carrier density achievable by gating. Figure 3 also shows that not only the GSP mode, but also the AR antimode, exhibits strong coupling with QW ISBT. This may be attributed to their common periodicity-induced origins [36]. This new superimposed states by AR and ISBT can be tentatively termed as intersubband antipolaritons, but the antipolaritons require further systematic studies for better understanding.

To elucidate the mechanisms of the different interaction behavior of the ISBT with LSP and GSP, the electric field

profiles are shown in Fig. 4a–c ($f = f_{\text{GSP}}$) and Fig. 4d–f ($f = f_{\text{LSP}}$). The arrow plot in Fig. 4a shows that the field in the GSP mode is mostly concentrated in the sandwiched region. However, as shown in Fig. 4d, the LSP mode penetrates the open region and spreads considerably into free space. As a result, the LSP mode exhibits a considerably larger radiation loss and a smaller Q -factor than the GSP mode. This agrees well with the observed narrow (broad) bandwidth of the GSP (LSP) transmission peak in Fig. 2.

The distinctive spatial field distributions can also be found in the xy -plane or QW-plane. As shown in Fig. 4b, the GSP mode forms stripe-like patterns due to their periodicity-induced propagating surface plasmon origin. In contrast, the field of the LSP mode is mainly confined within the open region because of its localized shape resonance nature (Fig. 4e). It should be pointed out that the E_z component of the GSP mode (Fig. 4c) has almost the same pattern and amplitude as the total field E , and both of them reach the same maximum value of ~ 100 (Fig. 4b, c). This suggests that the

Table 1 The field enhancement factors averaged over one unit-cell in xy -plane with $z=0$ (i.e., middle of the sandwiched semiconductor layer)

	$\langle E ^2 \rangle / E_0 ^2$	$\langle E_y ^2 \rangle / E_0 ^2$	$\langle E_z ^2 \rangle / E_0 ^2$	$\langle E_z ^2 \rangle / \langle E ^2 \rangle$
GSP	30.54	0.218	30.32	99.28 %
LSP	4.00	3.94	0.0617	1.54 %

normal incident light is efficiently converted from TE to TM polarization. This unique polarization conversion matches the polarization requirement of the QW ISBT excitation. However, concerning the LSP resonance (Fig. 4e, f), the maximum values of E and E_z differ by more than two orders in magnitude (~36 for E and ~0.15 for E_z), suggesting a very low polarization conversion ratio. In addition, the E_z component in Fig. 4f also shows also a stripe-like distribution, implying that the allowed interaction between the LSP and QW (Fig. 2c) derives essentially from the small scattered propagating surface plasmon portion [37]. To be more precise, we consider the area averaged field enhancements over the QW plane when evaluating the interaction strength between QW and plasmonic resonances [37]. Table 1 shows the calculated results for both the GSP and LSP modes. The total field enhancement factor in the LSP mode is about 1 order of magnitude lower than that in the GSP mode, while the E_z enhancement factor differs by almost 3 orders of magnitude. The polarization-conversion-ratio reaches near unity (~99.28 %) in the GSP mode but only ~1.54 % in the LSP one. In brief, both the large Q -factor and high polarization-conversion-ratio are responsible for the observed strong coupling between the GSP mode and QW ISBT. In other hybrid systems, although the exact quantitative results may change depending on the specific polarization and anisotropy of the interacting quantum transitions and plasmons, we believe that the main conclusion here is common to all PMI systems. Our results are therefore valuable to the design of hybrid MTMs coupled with quantum media in general and provide information on how to prepare tunable NRI materials by adopting the strong coupling effect in PMI.

Finally, we mention that an additional freedom can be introduced by applying different biases to the top and bottom metal layers with respect to the spacing QWs. With carefully designed QWs, this new freedom will hopefully drive the device into the ISBT gain region in order to achieve quantum cascade lasers [35, 38].

Summary

A novel optoelectronic metamaterial composed of the metallic DF structure and semiconductor QWs is investigated. The GSP and LSP exhibit dramatically a different coupling behavior with the QW ISBT, due to their distinctive resonance Q -factors and polarization-conversion-ratios. Our results provide insight into the physical mechanism of optoelectronic-coupled MTMs and pave the way for tunable optical applications of NRI materials.

Acknowledgement This work was jointly supported by the National Basic Research Program of China grant no. 2009CB929300, the NSFC contract nos. 10804019/11174055/60990321, Shanghai Science and

Technology Committee contract no. 09dj1400103, as well as Hong Kong Research Grants Council (RGC) nos. 112510 and 112212. We thank Dr Qiong He and Shiyi Xiao for valuable discussions.

References

1. J. Weiner, P.-T. Ho (2003) Light-matter interaction, fundamentals and applications, vol. 1 edn. (March 10, 2003)
2. Gibbs HM, Khitrova G, Koch SW (2011) Exciton-polariton light-semiconductor coupling effects. *Nat Photonics* 5:273
3. Zhang J, Tang Y, Lee K, Yang M (2010) Tailoring light-matter-spin interactions in colloidal hetero-nanostructures. *Nature* 418:91–95
4. Fontcuberta A, Stellacci F (2012) Light-matter interactions: Ultrastrong routes to new chemistry. *Nat Mater* 11:272–273
5. Oulton RF, Sorger VJ, Zentgraf T, Ma R-M, Gladden C, Dai L, Bartal G, Zhang X (2009) Plasmon lasers at deep subwavelength scale. *Nature* 461:629–632
6. Chen H-T, Padilla WJ, Zide JMO, Gossard AC, Taylor AJ, Averitt RD (2006) Active terahertz metamaterial devices. *Nature* 444:597–600
7. Engel M, Steiner M, Lombardo A, Ferrari AC, Löhneysen H, Avouris P, Krupke R (2012) Light-matter interaction in a microcavity-controlled graphene transistor. *Nat Commun* 3:906
8. Nussmann S et al (2005) Vacuum-stimulated cooling of single atoms in three dimensions. *Nat Phys* 1:122–125
9. Englund D, Faraon A, Fushman I, Stoltz N, Petroff P, Vuckovic J (2007) Controlling cavity reflectivity with a single quantum dot. *Nature* 450(7171):857–861
10. Cai W, Shalaev V (2010) Optical metamaterials: fundamentals and applications. Springer, New York
11. Shalaev VM (2007) Optical negative-index metamaterials. *Nat Photonics* 1:41–48
12. Pendry JB, Schurig D, Smith DR (2006) Controlling electromagnetic fields. *Science* 312(5781):1780–1782
13. Andersen ML, Stobbe S, Sørensen AS, Lodahl P (2011) Strongly modified plasmon-matter interaction with mesoscopic quantum emitters. *Nat Phys* 7:215–218
14. de Leon NP, Shields BJ, Yu CL, Englund DE, Akimov AV, Lukin MD, Park H (2012) Tailoring light-matter interaction with a nano-scale plasmon resonator. *Phys Rev Lett* 108:226803
15. Hess O, Pendry JB, Maier SA, Oulton RF, Hamm JM, Tsakmakidis KL (2012) Active nanoplasmonic metamaterials. *Nat Mater* 11(7):573–584
16. Zhang F, Zhang W, Zhao Q, Sun J, Qiu K, Zhou J, Lippens D (2011) Electrically controllable fishnet metamaterial based on nematic liquid crystal. *Opt Express* 19(2):1563–1568
17. Ricci MC, Xu H, Prozorov R, Zhuravel AP, Ustinov AV, Anlage SM (2007) Tunability of superconducting metamaterials. *IEEE Trans Appl Supercond* 17(2):918–921
18. Yi G-C (ed) (2012) Semiconductor nanostructures for optoelectronic devices. Springer, New York
19. Wuestner S, Pusch A, Tsakmakidis KL, Hamm JM, Hess O (2010) Overcoming losses with gain in a negative refractive index metamaterial. *Phys Rev Lett* 105(12):127401
20. Hamm JM, Wuestner S, Tsakmakidis KL, Hess O (2011) Theory of light amplification in active fishnet metamaterials. *Phys Rev Lett* 107:167405
21. Xiao S, Drachev VP, Kildishev AV, Ni X, Chettiar UK, Yuan H-K, Shalaev VM (2010) Loss-free and active optical negative-index metamaterials. *Nature* 466(7307):735–738
22. Bortolozzo U, Residori S, Huignard JPP (2010) Slow and fast light: basic concepts and recent advancements based on nonlinear wave-mixing processes. *Laser Photonics Rev* 4(4):483–498

23. Mary A, Rodrigo SG, Garcia-Vidal FJ, Martin-Moreno L (2008) Theory of negative-refractive-index response of double-fishnet structures. *Phys Rev Lett* 101:103902
24. Liu H, Capasso F (eds) (2000) Intersubband transitions in quantum wells: physics and device applications. Academic Press, New York
25. Todorov Y, Andrews AM, Sagnes I, Colombelli R, Klang P, Strasser G, Sirtori C (2009) Strong light-matter coupling in subwavelength metal-dielectric microcavities at terahertz frequencies. *Phys Rev Lett* 102:186402
26. Dini D, Köhler R, Tredicucci A, Biasiol G, Sorba L (2003) Microcavity polariton splitting of intersubband transitions. *Phys Rev Lett* 90:116401
27. Williams JB, Sherwin MS, Maranowski KD, Gossard AC (2001) Dissipation of intersubband plasmons in wide quantum wells. *Phys Rev Lett* 87:037401
28. Zhang X, Lin F (2010) Wedge mode of spoof surface plasmon polaritons at terahertz frequencies. *J Appl Phys* 108(11):113104
29. CONCERTO 7.0, Vector Fields Limited, England (2008)
30. Ortúñoz R, García-Meca C, Rodríguez-Fortuño FJ, Martí J, Martínez A (2009) Role of surface plasmon polaritons on optical transmission through double layer metallic hole arrays. *Phys Rev B* 79:075425
31. Smith DR, Schultz S, Markoš P, Soukoulis CM (2002) Determination of effective permittivity and permeability of metamaterials from reflection and transmission coefficients. *Phys Rev B* 65:195104
32. Zhang S, Genov DA, Wang Y, Liu M, Zhang X (2008) Plasmon-induced transparency in metamaterials. *Phys Rev Lett* 101:047401
33. Liu N, Langguth L, Weiss T, Kastel J, Fleischhauer M, Pfau T, Giessen H (2009) Plasmonic analogue of electromagnetically induced transparency at the Drude damping limit. *Nat Mater* 8:758–762
34. Sapienza L, Vasanelli A, Colombelli R, Ciuti C, Chassagneux Y, Manquest C, Gennser U, Sirtori C (2008) Electrically injected cavity polaritons. *Phys Rev Lett* 100:136806
35. Colombelli R, Ciuti C, Chassagneux Y, Sirtori C (2005) Quantum cascade intersubband polariton light emitters. *Semicond Sci Technol* 20(10):985
36. Wood RW (1935) Anomalous diffraction gratings. *Phys Rev B* 48:928–936
37. Wang H, An Z, Qu C, Xiao S, Zhou L, Komiyama S, Lu W, Shen X, Chu P (2011) Optimization of optoelectronic plasmonic structures. *Plasmonics* 6(2):319–325
38. Yao Y, Hoffman AJ, Gimach CF (2012) Mid-infrared quantum cascade lasers. *Nat Photonics* 6:432–439